



Design of Co-NC as efficient electrocatalyst: The unique structure and active site for remarkable durability of proton exchange membrane fuel cells

Kyungmin Im^{a,b,1}, Jue-Hyuk Jang^{b,1}, Jinseo Heo^{c,*}, Donghwi Kim^d, Kug-Seung Lee^e, Hyung-Kyu Lim^{c,*}, Jinsoo Kim^{a,d,**}, Sung Jong Yoo^{a,b,f,**}

^a KHU-KIST Department of Converging Science and Technology, Kyung Hee University, 26, Kyungheedaero-ro, Dongdaemun-gu, Seoul 02447, Republic of Korea

^b Center for Hydrogen • Fuel Cell Research, Korea Institute of Science and Technology (KIST), Seoul 02792, Republic of Korea

^c Department of Chemical Engineering, Interdisciplinary Program in Advanced Functional Materials and Devices Development, Kangwon National University, Chuncheon, Gangwon-do 24341, Republic of Korea

^d Department of Chemical Engineering (Integrated Engineering), Kyung Hee University, 1732, Deogyong-daero, Giheung-gu, Yongin-si, Gyeonggi-do 17104, Republic of Korea

^e Pohang Accelerator Laboratory (PAL), Pohang University of Science and Technology (POSTECH), Pohang, Republic of Korea

^f Division of Energy & Environment Technology, KIST School, University of Science and Technology (UST), Seoul 02792, Republic of Korea

ARTICLE INFO

Keywords:

Fuel cells
Spray pyrolysis
Composite materials
Oxygen reduction
Cobalt active site

ABSTRACT

Fe-N-C catalysts are promising alternatives to the platinum-group catalysts for use in oxygen reduction reactions of proton exchange membrane fuel cells. However, Fe-N-C catalysts suffer from poor durability, compared to non-precious metal catalysts, because of their accelerated demetallation by the Fenton reaction. In this study, we report the synthesis of a melamine-encapsulated Co-ZnO-C composite as a precursor and template for zeolite-imidazole-frameworks (ZIF-8). This approach allows formation of Co-N-C for constructing unique structures at meso- and macropore scales, while maintaining microporosity. Density functional theory analysis confirms the superior stability of the Co-N-C catalyst over other M-N-C catalysts (M = Fe, Ni, Cr, and Mn). Furthermore, it reveals that a closed interaction between the Co-N₄ moiety and organic adducts enhances oxophilicity, which prefers a 4-electron ORR activity. The Co-NC catalyst with a developed pore structure shows remarkable durability (6.7% performance degradation for 100 h) and full cell performance in H₂/O₂ under 1 bar of back-pressure (723 mW/cm² of maximum power density). Consequently, the unique structure of the synthesized catalyst successfully translates to the computationally-established ORR activity in the half-cell; superior durability is seen in the real device operation and stability analysis. This work is expected to support next-generation fuel cell development.

1. Introduction

Proton exchange membrane fuel cells (PEMFCs) are sustainable energy conversion systems. Owing to their carbon-free nature and high operational efficiency, they are widely believed to be suitable replacements of fossil fuels [1–3]. However, the oxygen reduction reaction (ORR) requires immense potential and therefore determines the rate-limiting steps for PEMFC operation [4]. Typically, platinum group metals (PGMs), and particularly, platinum-based catalysts have been commercialized as the cathode materials for the ORRs of PEMFCs.

However, the high cost of platinum-based catalysts is a key bottle-neck in the wider use of PEMFCs in hydrogen-based industries, such as public transportation, stationary power generation, and portable electronics. A novel catalyst with a metal-nitrogen-doped carbon (M-N-C) structure has been reported as a suitable replacement of the PGM catalysts in PEMFCs [5]. Recently, M-N-C catalysts doped with single-atomic-size metals have been studied for maximizing the ORR activity [6–9]. Among the single-atomic M-N-C construction methods, those based on metal-organic frameworks (MOFs) are the most widely used and straightforward ones, particularly, the zeolite-imidazole frameworks

* Corresponding authors.

** Corresponding authors at: KHU-KIST Department of Converging Science and Technology, Kyung Hee University, 26, Kyungheedaero-ro, Dongdaemun-gu, Seoul 02447, Republic of Korea.

E-mail addresses: hklm@kangwon.ac.kr (H.-K. Lim), jkim21@khu.ac.kr (J. Kim), ysj@kist.re.kr (S.J. Yoo).

¹ These authors contributed equally to this work.

<https://doi.org/10.1016/j.apcatb.2022.121220>

Received 19 November 2021; Received in revised form 30 January 2022; Accepted 12 February 2022

Available online 15 February 2022

0926-3373/© 2022 Elsevier B.V. All rights reserved.

(ZIF-8) [10–14]. MOFs are suitable for the synthesis of single atomic catalysts because they comprise organic ligands and inorganic metals in a regular arrangement with a large specific surface area. In addition, because the organic ligand of ZIF-8 consists of nitrogen element, N-doping can be facilitated during carbonization, and pores can be induced by using the low evaporation point of zinc metal in ZIF-8 [13, 15, 16]. Most ZIF-derived single-atomic catalysts are prepared using the following procedures: 1) conventional ZIF-8 synthesis methods, 2) ZIF-8 structure tuning, and 3) carbonization (pyrolysis) at high temperatures [17–20]. For the synthesis of single-atomic catalysts through this method, active metals are absorbed during the tuning process, trapped in the ZIF-8 pores, and heat-treated for developing the M-N-C. Recently, several groups have attempted coating the metal-absorbed ZIF-8 with silica (tuning the ZIF-8 structure), for preventing the shrinkage of the carbon frame during the high-temperature heat treatment, thereby maintaining a high specific surface area and preventing aggregation of active metals [21–23]. Wan et al. coated mesoporous silica on ZIF-8, and the Fe precursor was strongly absorbed into the pores after the heat treatment with silica etching. The large external surface area of the Fe-N-C from mesoporous silica provided a large number of active sites and efficient mass transport in the full-cell (MEAs) [24]. In addition to silica, single atomic Fe-N-C catalysts, possessing high specific surface area and various pore size distributions, were prepared using polymers such as polyaniline (PANI), phenanthroline (Phen), and polypyrrole (Ppy), and exhibited high fuel cell performance [25, 26]. Overall, to the best of our knowledge, development of the surface area and porosity of the catalyst are the key factors for MEA applications. Although several studies have reported that Fe-N-C catalysts offer superior performance compared to the Pt-based catalysts, most Fe-N-C catalysts have been mainly studied in alkaline media. While Fe-N-C catalysts also have good performance in acidic media, their poor stability limitations due to demetallation via the Fenton reaction, requires improvement [27, 28]. In comparison to the Fe-N-C systems, the Co-N-C catalysts have been reported to offer improved stability in acidic media owing to the resistance of cobalt to radical oxygen species (ROS). However, atomically-dispersed Co-N-C have been reported to preferentially operate via 2-electron ORR activity compared to the 4-electron ORR activity [29]. Therefore, design of cobalt catalysts that predominantly operate via the 4-electron reaction is necessary. Xie et. al. reported atomically dispersed a Co(mIm)-NC catalyst with high cobalt content (1.0 at%). They confined a cobalt into the micropore of ZIF-8 with 2-methylimidazole (mIm) for encapsulation of CoN₄ moieties. After carbonization of Co(mIm)₄@ZIF-8, Co(mIm)-NC achieved high ORR activity of 0.82 V(E_{1/2}) and a peak power density of 0.64 W/cm² in H₂/O₂ fuel cell conditions. Since cobalt (Co²⁺) coordinates with 2-methylimidazole of ZIF, Co-N-C having a high cobalt content can be prepared [30, 31]. We believe that the development of a single-atomic-size Co-N-C catalyst with high active site density is a promising approach for replacing iron and platinum-based catalysts that exhibit excellent 4-electron ORR selectivity and durability in full cells.

Continuing our work on ZIF-derived Co-N-C catalysts, we report herein a novel catalyst. In contrast to the reported methods, in the current approach, we attempted tuning the precursor in the first step by synthesizing a hollow melamine@Co-ZnO-C (melamine-encapsulated Co-doped ZnO, denoted as ma-Co-ZnO) composite as a ZIF precursor by spray pyrolysis. The ma-Co-ZnO prepared using the spray pyrolysis showed a unique structure in which melamine was not completely decomposed and remained in the ZnO sphere. This composite was converted to a melamine@Co-ZIF-8 composite (denoted as ma-Co-ZIF-8) using the pseudomorphic growth method, which allowed material conversion while maintaining the shape and dimensions of the original raw material. This synthesis strategy afforded ZIF-derived catalysts that did not suffer from the typical limitations of micro-porosity and a limited shape that lacks a hard or soft template. The prepared melamine@Co-ZIF-8 composite derived Co-N-C (denoted as ma-Co-NC) has both micro- and mesoporosity and a hollow structure with high

cobalt dispersion in the N-doped carbon frame. The melamine in the composite plays a crucial role as a mesopore-forming agent and carbon/nitrogen source, preventing cobalt agglomeration during high-temperature treatment. Above all, the formation of C/N/O covalent adducts from the melamine and ZnO sources affected the 4-electron ORR selectivity. This unique ma-Co-NC exhibited excellent performance and durability in a single cell (MEA). Theoretical analysis confirmed that the catalytic activity and stability originated from the enhanced oxophilicity of the Co-N₄ active site toward the axial coordination environment and the higher demetallation energy compared to the other transition metals.

2. Experimental section/methods

2.1. Chemicals

Zinc nitrate hexahydrate (Zn(NO₃)₂·6H₂O, 98%), cobalt chloride hexahydrate (CoCl₂, 97%), melamine, 2-methylimidazole (C₄H₆N₂, 98%), and Nafion solution (5 wt% Nafion in alcohols and water) were sourced from Sigma-Aldrich, Korea. DMF (HCON(CH₃)₂, 99.5%) and methanol (CH₃OH, 99.5%) were purchased from Daejung, Korea. DI water was produced using Aqua Max Ultra 360 (Younglin, Korea).

2.2. Synthesis of ma-Co-NC catalyst

Mealmine@Co-ZnO-C (ma-Co-ZnO) precursors were synthesized by ultrasonic spray pyrolysis. Zinc nitrate hexahydrate (6.07 g) was dissolved in 200 ml DI water, and 0.237 g of cobalt chloride hexahydrate was dissolved in 5 ml methanol until a transparent solution was obtained. After stirring for 10 min, the zinc and cobalt solutions were mixed and heated at 50 °C with stirring. 2.52 g of melamine was added to the mixed solution at 50 °C for 1 h. The prepared solution was transferred to a nebulizer and atomized to a droplet. The generated droplet was transferred to a quartz-covered electrical furnace using an inert gas. The furnace temperature and gas flow were fixed at 500 °C and 6.6 L/min. The final product was collected in a thimble filter at 170 °C to prevent condensation. For conversion to MOF (ZIF-8), 0.392 g of ma-Co-ZnO was dispersed in 45 ml DMF, and 0.796 g of 2-methylimidazole was dissolved in 15 ml DI water for 30 min. The dispersed mealmine@Co-ZnO-C solution was added to the 2-methylimidazole solution and mixed for 24 h at 25 °C. After conversion, mealmine@Co-ZIF-8 (ma-ZIF-8) was washed with methanol thrice and dried at 70 °C in a convection oven for 12 h. In the final step, ma-ZIF-8 was placed in an electrical furnace and carbonized at 900 °C for 2 h.

2.3. Characterization

Scanning electron microscopy (FE-SEM; Merlin, Carl Zeiss) was used to measure the morphologies of the precursor and final product. Transmission electron microscopy (HR-TEM, Talos F200X, FEI) and scanning transmission electron microscopy (STEM, TitanTM 80–300, FEI) were used to measure the morphology of the precursor and final product and distribution of elements. Nitrogen isotherms and pore size distributions were analyzed by Brunauer-Emmett-Teller analysis (BET, Belsorp-max, MicrotraBEL) and mercury pressure porosity (AutoPore V, Micromeritics) were used to measure the BET surface area and pore size of the precursor and final product. X-ray absorption fine structure (XAFS) measurements were performed to probe the valence state and the coordination of cobalt species at the 8 C nano-probe XAFS beamline (BL8C) of the Pohang Light Source (PLS-II) in the 3.0 GeV storage ring, with a ring current of 360 mA. XAFS spectra were collected in fluorescence mode. The obtained spectra were processed using Demeter software. Extended x-ray absorption fine structure (EXAFS) spectra were fitted in a Fourier-transform range of 3–14 Å^{−1} with a Hanning window applied between 1.0 Å and 2.7 Å. The amplitude reduction factor (S₀²) was set to be 0.85.

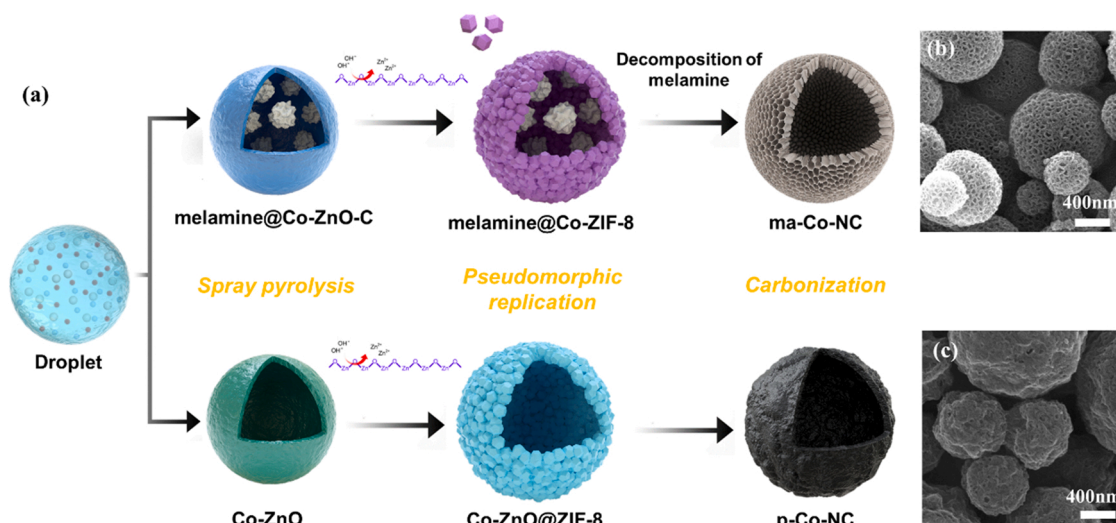


Fig. 1. (a) Schematic for synthesis of ma-Co-NC (melamine added Co-NC) and p-Co-NC (pristine Co-NC) by spray pyrolysis, pseudomorphic replication (convert to MOF), and carbonization at 900 °C. Melamine partially decomposes during the spray pyrolysis process and completely decomposes in carbonization. SEM images of (b) ma-Co-NC and (c) p-Co-NC.

All electrochemical devices were fabricated in a three-electrode system using an RDE. A saturated calomel (SCE) electrode was used as the reference electrode, and graphite rod was used as the counter electrode (Autolab potentiostat, Metrohm). A 0.196 cm² glassy carbon (GC) electrode was used as the working electrode, and the catalyst was supported on GC. In this study, 5 mg of catalyst and 30 µL of Nafion solution (5 wt% Nafion solution) were dispersed evenly in 400 µL of isopropanol using sonication and stirring. ORR and CV measurements were performed by purging oxygen and argon in a 0.5 M H₂SO₄ electrolyte. ORR activity was performed over a potential range of 0.1–1.0 V at 5 mV/s. The SCE electrode was converted to potentials versus the reversible hydrogen electrode (RHE), and the currents were normalized to the current densities using the geometric area of the electrode. The uncompensated resistance was calculated using impedance analysis. The prepared ink was dropped onto the glassy carbon electrode surface and used as the working electrode. (Loading amount of the ink is 0.8 mg/cm²). Potential cycle test for durability of catalyst was performed in potential range between 0.6 and 1.0 V at 100 mV/s for 10,000 cycles.

2.4. MEA fabrications and single cell tests

MEA was prepared by a hand-spraying method with a catalyst-coated membrane (CCM). In the catalytic ink, the catalyst ionomer (Nafion®, Sigma Aldrich) was dispersed ultrasonically for 1 h. The anode was used at 0.2 mg/cm² by applying commercial Pt/C (JM Pt/C, 40 wt.% Pt). The cathode was loaded with the synthesized catalyst; the amounts ranged from 1.0 to 4.0 mg/cm². The prepared MEAs were sandwiched between the gas diffusion layers (GDLs, 39 BCE, SGL) to construct a single cell for the operation. The fuel cell was tested using fully humidified gases such as H₂ and O₂ at 80 °C in a fuel cell station (CNL, Korea). The i-V polarization curves were measured by adjusting the current density from the OCV to 0.3 V. The stability test was conducted for 100 h based on the changes in the current density at 0.7 V. The dissolution rate was estimated by measuring the amount of metal in the catalyst coating film (CCM) using ICP-OES and how much the amount decreased before and after the stability test.

2.5. Computational methods

We performed spin-polarized DFT calculations using the Vienna Ab-initio Simulation Package (VASP) [32] with the Perdew–Burke–Ernzerhof exchange-correlation functional of Perdew–Burke–Ernzerhof

(PBE) [33]. The electron-ion interaction was considered in the form of the projector-augmented-wave (PAW) method with a plane wave up to a cutoff energy of 400 eV. The 4 × 4 supercells of the hexagonal graphene structure were used to generate the TM-N₄ catalyst models. The Brillouin zone was sampled using a gamma-centered 4 × 4 × 1 k-point mesh. A 15 Å vacuum layer and a dipole correction scheme along the z-axis were applied to avoid electrostatic interactions between neighboring images across the periodic boundary. The free energy of the PCET step was calculated by using the reference to the free energy of gaseous H₂, following the CHE scheme developed by Nørskov et al [33]. The electronic energy of O₂ was modified by −0.18 eV to reproduce the overall ORR thermodynamics (+1.23 V vs. SHE) correctly. The free energy of the aqueous state was calculated using the VASPOL code developed by Hennig et al [34]. The same vibrational and solvation free energy terms calculated from the ideal Co-N₄ catalyst were applied to the other catalyst models.

3. Results and discussion

3.1. Catalyst synthesis

Coral-shaped Co-NC (ma-Co-NC) was synthesized by combining ultrasonic spray pyrolysis, pseudomorphic growth, and carbonization. First, we prepared the hollow structural melamine@Co-ZnO-C (melamine-encapsulated Co-doped ZnO, ma-Co-ZnO) to easily tune the catalyst. Melamine partially decomposed to carbon and was encapsulated in the Co-doped ZnO-C sphere because of its short residence time in the ultrasonic spray pyrolysis process (2 s). The synthesized melamine@Co-ZnO-C was used as the MOF precursor and as a template for melamine@Co-ZIF-8 (ma-Co-ZIF-8). The synthesis mechanism in this process relies on the amphoteric properties of ZnO, owing to which, it is easily soluble in both basic and acidic environments. 2-Methylimidazole plays a crucial role in promoting ZnO dissolution, by acting as a base, and combines with the dissolved Zn²⁺ to form polycrystalline ZIF-8. Using this strategy, we were able to synthesize a melamine-encapsulated ZIF-8 composite without segregation of particles [35–37]. In the final carbonization step, the remaining melamine decomposed completely during the ma-Co-ZIF-8 pyrolysis. The generated NH₃ gas formed new kinds of pores on the surface (Fig. 1(b)), and melamine, as a carbon source, prevented the aggregation of cobalt in the Co-NC structure even at high temperatures (900 °C).

We confirmed that melamine was encapsulated in the ZnO and ma-

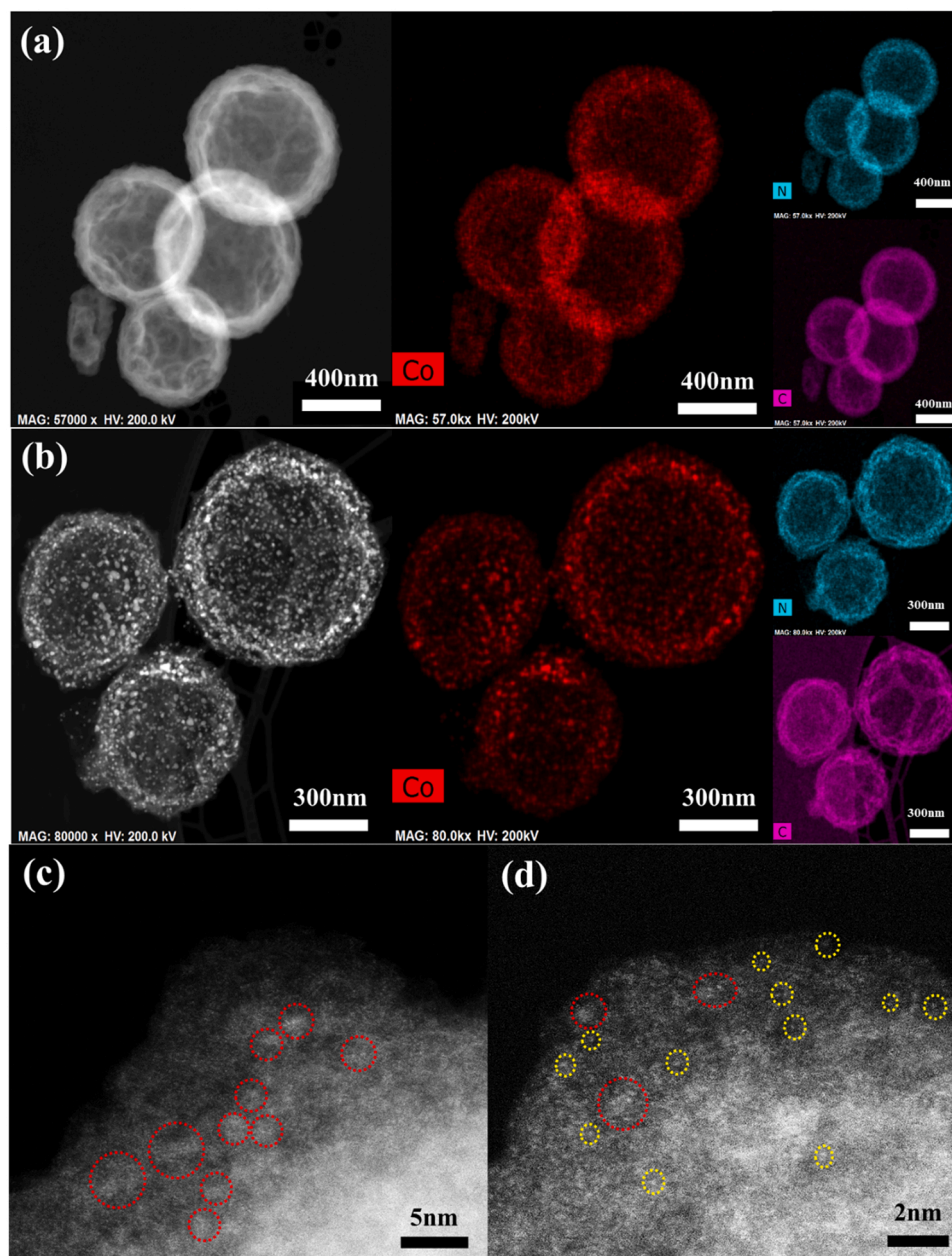


Fig. 2. HADDF-TEM image of (a) ma-Co-NC and (b) p-Co-NC and their elemental mapping images of cobalt, nitrogen, and carbon. (c) HADDF-STEM image and (d) the magnified images of ma-Co-NC at the atomic size level.

Co-ZIF-8 hollow spheres, from the TEM image in Fig. S2. The SEM images (Fig. S3) indicate that ma-Co-ZnO and ma-Co-ZIF-8, which were added with melamine, became more spherical due to the decomposition of melamine into the carbon. As shown in Fig. S1(a), the XRD patterns of ma-Co-ZIF-8 indicated conversion from ZnO to ZIF-8, unlike in the melamine-free sample (p-Co-ZIF-8), which was confirmed to have a composition of approximately 35% ZIF-8 phase and 65% ZnO phase. Consistent results were also confirmed by the nitrogen isotherm plot in Fig. S1(c) and Table S1. The specific area of ma-Co-ZIF-8 had a similar result to the typical ZIF-8 particles at 1229.8 g/cm², whereas p-Co-ZIF-8 had a relatively low specific surface area of 883.6 g/cm². It is estimated that p-Co-ZIF-8 contains a large amount of dense ZnO, which results from the difference in the ZnO density between the two samples. When ZIF-8 grows on the ZnO surface, it acts as a barrier through which the dissolved zinc ions cannot pass, thus limiting the conversion to ZIF-8. However, as mentioned above, the partially decomposed melamine present between the crystals of ma-Co-ZnO, lowers the density of ZnO.

Even if ZIF-8 grows on the ZnO surface, the presence of melamine promotes the movement of zinc ions, resulting in the smooth synthesis of ZIF-8. In Fig. S1(d), the ZnO peak decreased with increasing melamine concentration. This indicates that melamine affects the conversion of the ZIF phase.

HR-TEM and elemental mapping images of ma-Co-NC and pristine Co-NC (p-Co-NC) are shown in Fig. 2 to explain the melamine effect after carbonization. As shown in Fig. 2(a)–(b), ma-Co-NC and p-Co-NC showed hollow and spherical particles due to the precursor of the ZnO hollow sphere. However, ma-Co-NC had a high cobalt dispersion, and no cobalt species agglomerated in ma-Co-NC were detected in the elemental mapping image compared to that of p-Co-NC because of the effect of melamine. High-angle annular dark-field (HAADF)-STEM was analyzed to probe the cobalt species in the ma-Co-NC, and atomic cobalt clusters of ma-Co-NC are shown in Fig. 2(c)–(d). Other regions were also investigated to identify cobalt species (Fig. S6–S9). Most cobalt species exist as an atomic cluster or single-atomic, but it has also been observed

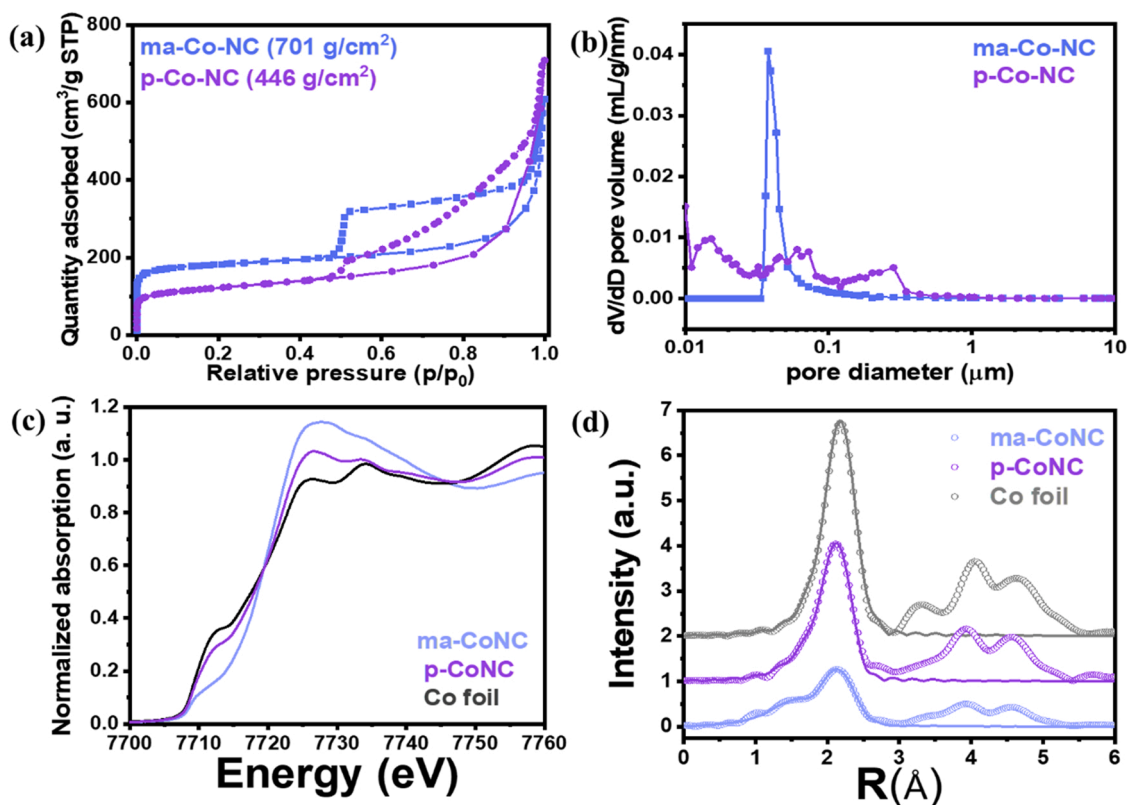


Fig. 3. Textural properties of (a) nitrogen isotherm plots and (b) pore size distribution plots for ma-Co-NC and p-Co-NC. Pore size distribution plots were measured using mercury porosimetry. (c) XAS spectra Co K edge XANES and (d) experimental EXAFS spectra and fitting spectra of ma-Co-NC and p-Co-NC. (The dots represent the experimental spectra, and the lines represent the fitting spectra).

that it exists in metallic phase (2–3 nm). These results confirm the XRD results that ma-Co-NC has carbon peaks alone, as shown in Fig. S1(b). The textural properties of ma-Co-NC and p-Co-NC were measured to confirm the hierarchical structure of ma-Co-NC in Fig. 1(b) by N₂ adsorption-desorption isotherms and mercury porosimetry (Fig. 3(a) and (b)).

The BET surface area of ma-Co-NC (689.9 m²/g) was much higher than that of p-Co-NC (436.7 m²/g) owing to the higher BET surface area of ma-Co-ZIF-8 precursor, which is completely converted to ZIF from ZnO. Examination of the mesopores in the N₂ isotherm curves indicated the presence of mesopores in the structure, evidenced by the hysteresis loop. ma-Co-NC and p-Co-NC both showed hysteresis loops, which are attributed to zinc evaporation during the carbonization step and hollow structure. Melamine also affected the formation of a hysteresis loop in the case of the ma-Co-NC catalyst. In addition, mercury porosimetry measurements were performed to carefully measure the mesopores and macropores on the catalyst surface (Fig. 3(b)). p-Co-NC showed an irregular pore size distribution. However, ma-Co-NC demonstrated unimodal mesopores and a high intensity at 38 nm. We believe that this unique pore structure can affect the catalytic performance, especially in full cell performance (MEAs). X-ray absorption spectroscopy (XAS) spectra of ma-Co-NC, p-Co-NC, and a reference (Co foil) were measured to probe the oxidation state and the coordination of cobalt species, as shown in Fig. 3(c)–(d). The pre-edge peak near 7712 eV decreased for the Co foil, p-Co-NC, and ma-Co-NC, and the white line near 7725 eV showed the opposite trend, indicating that the cobalt species in the ma-Co-NC had a higher oxidation state than those of p-Co-NC and Co foil; p-Co-NC had a higher oxidation state than that of Co foil. The EXAFS fitting results of the ma-Co-NC catalyst revealed the various interactions of N and C with Co. Calculations indicated the presence of four phases in ma-Co-NC—Co-N_(CN = 4) (coordination number = 4), Co-C_(CN = 2), and the two kinds of Co-Co_(CN = 5). Further, p-Co-NC showed Co-N_(CN = 4) and Co-

Co-N_(CN = 5) phases. Interatomic distances of Co-N, Co-C, and two kinds of Co-Co in ma-Co-NC were 1.94, 2.22, 2.49, and 2.83 Å, respectively (Table S3). As mentioned in the XANES analysis, in the EXAFS spectrum (Fig. 3(d)), ma-Co-NC demonstrated a high oxidation state (less metallic phase), and hence the Co-Co peak intensity near 2.1 Å was much lower than that of p-Co-NC. Conversely, ma-Co-NC demonstrated a high intensity for the Co-N peak near 1.5 Å. Therefore, it is suggested that the ma-Co-NC catalyst exhibits high cobalt dispersion and coordination with N, C, and Co from the EXAFS fitting results. This coordination is due to the use of melamine@Co-ZnO-C as the precursor. Considering the STEM results and the measured Co-Co phase in ma-Co-NC, cobalt exists as an atomic cluster and nanocluster (2–3 nm). However, since the metallic phase is rarely observed in STEM analysis, it exists in a very small amount. (metallic phase is not observed in XRD of Fig. S1.) ICP-OES revealed that the cobalt loading in ma-Co-NC was 4.01 wt%, higher than that reported in previous studies on single-atomic catalysts (<1 wt %) [38,39]. Therefore, we believe that a small amount of metallic phase is observed due to the high loading amount, but most of them exist as atomic clusters. Our unique approach, which increases the density of the cobalt sites, is suitable for improving the 4-electron ORR performance, as cobalt tends to exhibit 2-electron and 4-electron reactions simultaneously.

3.2. Catalyst activity and stability

As shown in Fig. 4(a), the ORR activity of ma-Co-NC and the p-Co-NC catalyst was evaluated in 0.5 M H₂SO₄. ma-Co-NC showed a higher ORR activity than that of p-Co-NC. ma-Co-NC showed a higher ORR activity than that of p-Co-NC. This is ascribed to a high surface area and metal dispersion due to the influence of melamine. Additionally, ma-Co-NC showed a 4-electron pathway and a low H₂O₂ yield (4.8% at 0.7 V) when ma-Co-NC were loaded at 47.4 μg/cm² for accurate H₂O₂ yield

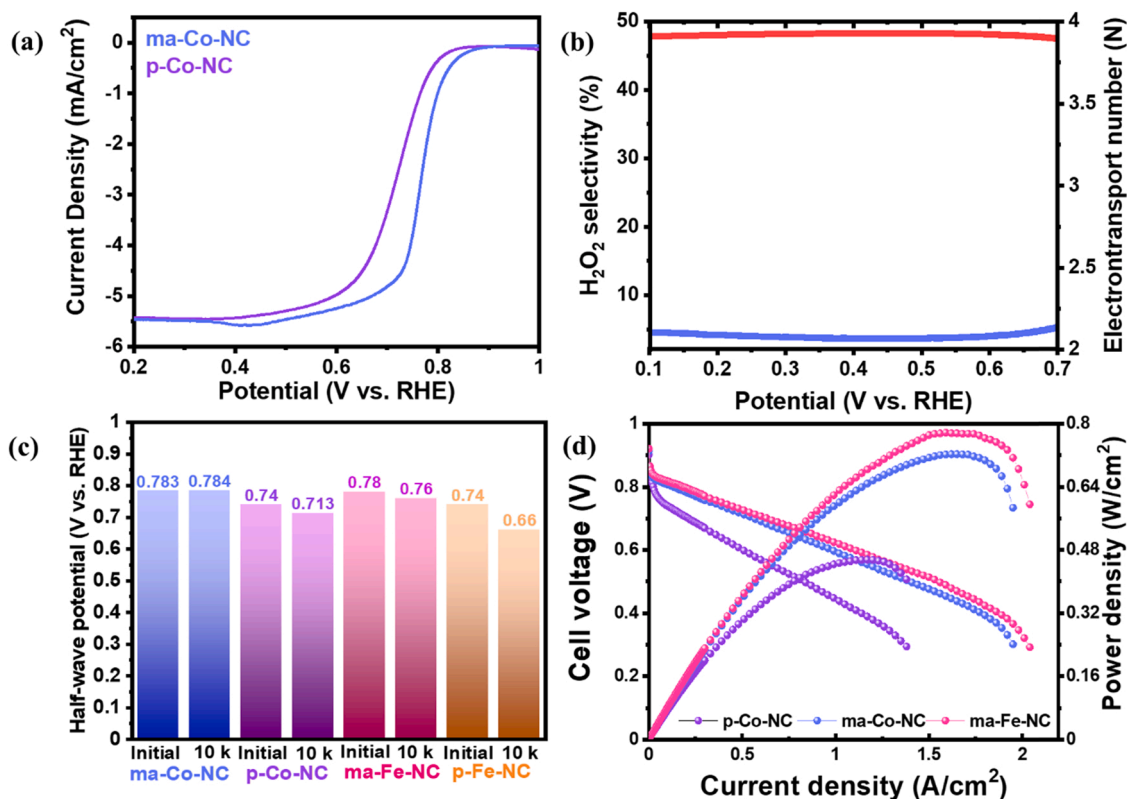


Fig. 4. (a) ORR polarization plot of ma-Co-NC and p-Co-NC in O₂-saturated 0.5 M H₂SO₄ electrolyte (5 mV/s scan rate). (b) H₂O₂ yield and electron transport number for ma-Co-NC. (c) comparison of half-wave potential for ma-Co-NC, p-Co-NC, and ma-Fe-NC (atomically dispersed Fe-NC) before and after potential cycle test. (d) H₂/O₂ Fuel cell performance of ma-Co-NC, p-Co-NC, and ma-Fe-NC.

measurements [29]. Durability test of the four kinds of homemade catalysts was performed by conducting the cycling test between 0.6 and 1.0 V in O₂-saturated 0.5 M H₂SO₄ (Fig. 4(c)-(d), Fig. S9). To compare iron-based catalysts, which have high reported ORR activities, we prepared highly dispersed Fe-NC (ma-Fe-NC) and nanosized Fe-NC (p-Fe-NC), such as ma-Co-NC and p-Co-NC (Fig. S9 and Fig. S10). ma-Co-NC exhibited no degradation in the half-wave potential after 10,000 cycles. p-Co-NC showed a loss of 27 mV after the durability test, and ma-Fe-NC showed a 20 mV loss. However, its durability is better than that of p-Co-NC owing to the high dispersion of Fe in the carbon. In the case of p-Fe-NC, an 80 mV loss was observed after the durability test. This trend indicates that the use of atomic clusters or single-atom catalysts is an appropriate strategy for improving the durability and performance of the M-N-C catalysts, and that the cobalt-based catalysts are more stable than iron-based catalysts under acidic conditions, regardless of the metal size. MEAs were fabricated using the prepared electrocatalysts for application as cathode catalysts in PEMFCs. The performance of the single-cell was measured by controlling the current density from OCV to 0.3 V. The single-cell performances of the catalysts (p-Co-NC, ma-Co-NC, and ma-Fe-NC) are shown in Fig. 4(d) and Fig. S13. The optimized performance according to the catalyst loading, ionomer content, and backpressure is shown in Fig. S12. The MEA performance was optimized by applying a back pressure of 1 bar at a catalyst loading of 4 mg/cm² and an ionomer content of 35 wt% (ionomer contents = ionomer / (ionomer + catalysts)). The current density at 0.6 V was 510, 990, and 1110 mA cm⁻² for p-Co-NC, ma-Co-NC, and ma-Fe-NC, respectively, and the maximum power densities were 455, 723, and 776 mW/cm², respectively. The power density of the ma-Co-NC was 37% higher than that of p-Co-NC, which is similar to their ORR activity in the half-cell conditions. This is a change in activity due to the developed pore structure and metal dispersion in ma-Co-NC [12,24]. The performance of the ma-Fe-NC was approximately 6.8%

higher than that of the ma-Co-NC. Fe-based catalysts generally show higher performance than Co-based catalysts (Fig. S10), and the gap in the performance of the Co-NC and the Fe-NC catalysts is becoming narrow.

The single-cell durability of the synthesized catalysts driven at 0.7 V for 100 h is shown in Fig. 5(a). The durability (performance decay) of p-Co-NC, ma-Fe-NC, and ma-Co-NC was 58.6%, 48.4%, and 6.7%, respectively. The difference in durability between the nanoparticle-based catalysts and atomic cluster-based catalysts was confirmed by the Co metal dissolution rate (Fig. 5(b)). Co nanoparticles in p-Co-NC dissolved approximately 60% during the stability tests, but the Co atomic cluster-structured catalysts (in ma-Co-NC) recorded a metal dissolution rate of less than 8%. Thus, it was proved that metal particles having a single atom or cluster structure, in comparison to those of the nanoparticles, effectively prevent metal decomposition during fuel cell operation and contribute to improved durability. Meanwhile, Fe deterioration was observed in the atom cluster structure. In particular, the Fe metal dissolution was 20%, which was three times higher than that for the Co metals. The deteriorated catalysts had a severe effect on the durability and activity of the Fe-based catalysts. DFT calculations confirmed the superior stability of the Co-NC catalyst over that of Fe-NC in experiments, which can be attributed to the fact that Co-NC offers the greatest resistance to the dissolution of the central metal ion into the electrolyte via demetallation [40–42]. In the DFT calculations, the demetallation process was assumed to be an aqueous reaction, in which the central metal ions from the TM-N₄ (TM: transition metal) catalyst are dissolved by water molecules, leaving the empty []-N₂(NH)₂ active site (Eq. 1). Since the TM-N₄ macrocyclic moiety has an oxidation state of TM²⁺, the dissolution energies of TM³⁺ ions were calculated by taking *OH as the initial state (Eq. 2). The reaction energies of the demetallation process were calculated for the five major TMs based on the Born-Haber cycle (Fig. S14, Table S4), and the results are presented in

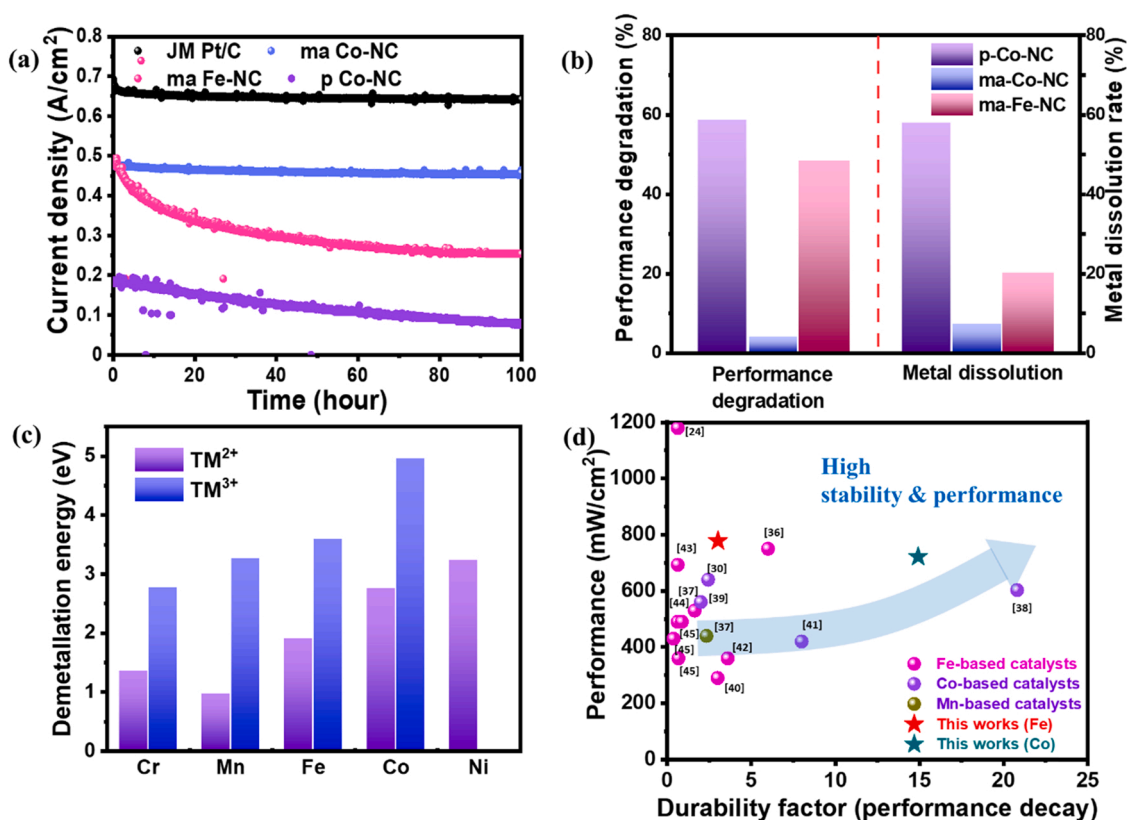


Fig. 5. (a) Single cell durability test at a constant potential of 0.7 V for ma-Co-NC and commercial Pt/C during 100 h. (b) Single cell performance degradation and metal dissolution rate before and after stability test for p-Co-NC, ma-Co-NC, and ma-Fe-NC. (c) Calculated demetallation energy of each transition metal ion from TM-N₄ active sites. (d) Comparison of fuel cell performance related with durability for transition metal based catalyst (durability factor = 1/(loss %/hour)) [24, 30,44–53].

Fig. 5(c). The higher the reaction energy, the more difficult it is for the transition metal to dissolve out from the active site. The stability against demetallation tended to improve as the number of *d* electrons in the TMs increased. Among the TM²⁺ ions, Mn-N₄ was the easiest to dissolve, while Ni-N₄ was the most difficult, which is consistent with the previously reported experimental results of demetallation from metal porphyrin species [43]. Overall, after accounting for the clear stability trend of TM³⁺ ions, we confirmed that Co-N₄ has superior stability against dissolution over Fe-N₄ because of the intrinsic bonding nature of TM-N₄. Considering each energy component of the Born–Haber cycle, the energy costs of breaking the TM–N and TM–OH bonds (ΔE_3 and ΔE_5 in Table S4, respectively) are the dominant factors in determining the tendency of the demetallation process.

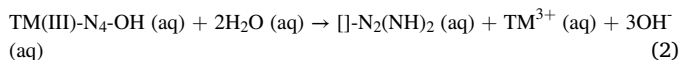
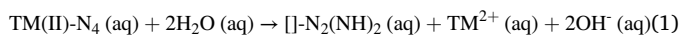


Fig. 5(d), primarily demonstrating the research reported since 2010, clearly showed the high activity of the Fe-based catalyst and the severe problem of durability in the single-cell systems. The Co-based catalyst showed slightly lower performance than Fe, but the performance decay per hour (durability) was improved to about 1/4. In particular, the developed ma-Co-NC catalyst exhibited superior durability compared to non-precious metal-based catalysts during stability tests in single-cell conditions.

3.3. Origin of enhanced ORR activity in Co-NC catalyst

DFT calculations were performed to determine the cause of the enhanced 4-electron ORR activity of the ma-Co-NC catalyst. First, as

shown in Fig. 6(a), the free energy profiles of the associative ORR pathway for the bare Co-N₄ and bare Fe-N₄ active sites were obtained under an applied potential of + 0.66 V vs. a computational hydrogen electrode (CHE), which is the equilibrium potential for H₂O₂ production. Bare Co-N₄ was found to have a weaker oxophilicity than Fe-N₄ for all reaction intermediate species (i.e., *O₂, *OOH, *O, and *OH). In particular, the *OOH state, generated by the first proton-coupled electron transfer (PCET) step in CoN₄, is located at a higher energy level than that of the H₂O₂ state, thereby increasing the favorability of the 2-electron ORR [29]. Therefore, from a theoretical point of view, the dominant 4-electron ORR activity of the ma-Co-NC catalyst is postulated to be derived from the specific coordination environment of the Co-N₄ active site, which provides stronger *OOH binding. The most significant difference in the active site structure between the ma-Co-NC and p-Co-NC catalysts lies in the different coordination environments around the Co-active site and the presence or absence of Co nanoparticles (Co-NPs), which can be estimated based on EXAFS and XPS analysis results. The p-Co-NC catalyst contains many Co-NPs of approximately 10 nm size and is therefore likely to interact closely with the Co-N₄ active site. In contrast, the active site on the ma-Co-NC catalyst is believed to interact closely with various C/N/O covalent adducts formed on the surface of the carbon support from melamine@Co-ZnO-C composite during the synthesis. The contact between Co and C/N was measured in XPS and EXAFS results (Table S2 and S3). These contacts appeared mainly in melamine-added Co-NC. We determined the effect of the different coordination environments on the characteristics of the Co-N₄ active site in terms of the distances, using DFT based on the various types of axially coordinated structures with organic molecules and Co atomic clusters. Six types of coordination structures with organic molecules were modeled: ethane and benzene for Co–C contact, DMA and DMHA for Co–N contact, and DME and DMHA(O) for Co–O contact. The

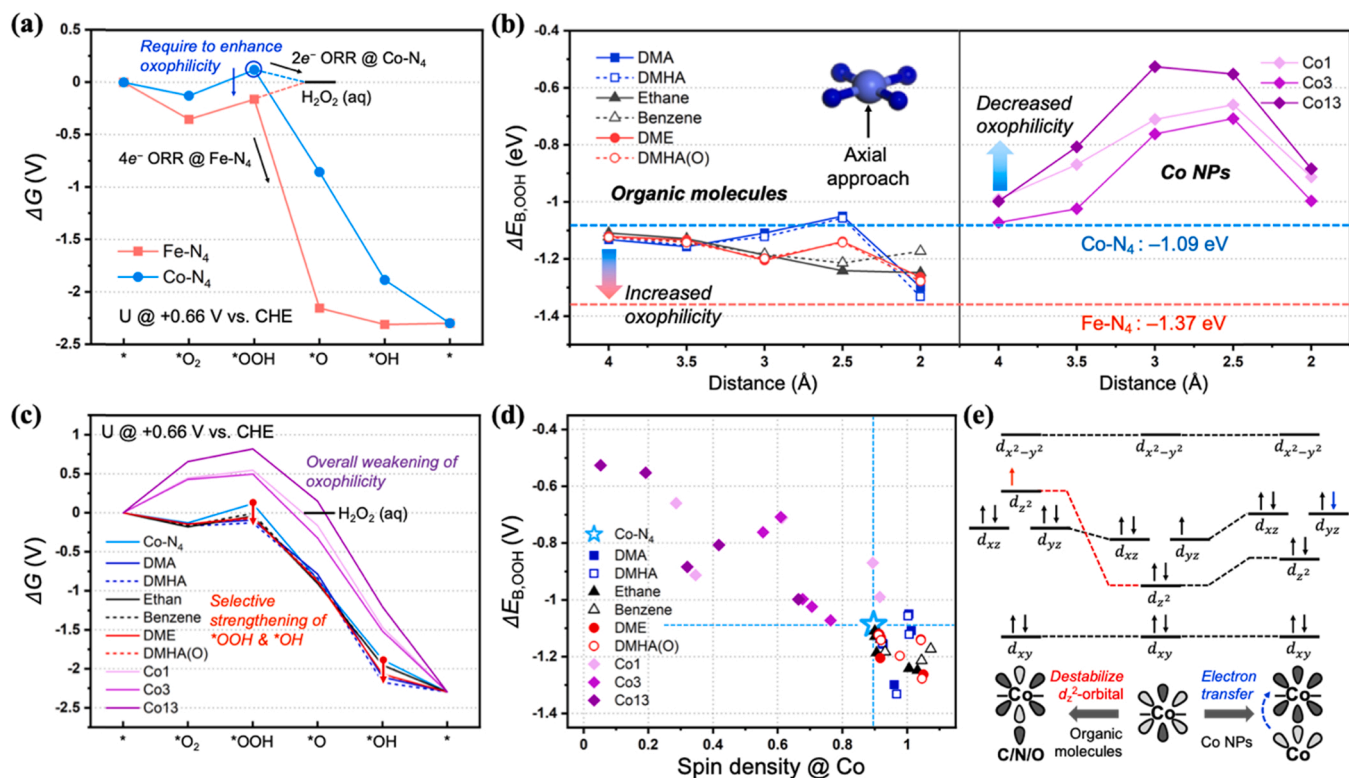


Fig. 6. (a) Calculated free energy profile of associative ORR pathway for bare Co-N₄ and Fe-N₄ active sites. (b) Effect of axial-coordination on *OOH binding strength according to chemical species and distances. (c) Calculated free energy profile for each axial-coordinated structure that has maximum or minimum *OOH binding energy. (d) Correlation between spin density at Co active site and *OOH binding energy. (e) Schematic molecular orbital diagram for axial-coordinated structure based on crystal field theory.

interactions with Co-NPs were modeled using a Co nanocluster composed of one, three, and 13 Co atoms (Co1, Co3, and Co13, respectively). The changes in the electronic structure and ORR activity were analyzed by scanning the axial interaction distance between the Co-N₄ active site with organic molecules or the Co nanocluster from 4 to 2 Å in 0.5 Å intervals in the axial direction (Fig. S15). The plot of the *OOH binding energy with respect to the coordination distance is shown in Fig. 6(b). For coordination with organic molecules, the overall binding energy increased as the distance decreased. The maximum binding energy depended on the interacting chemical species, with a maximum value of 2 Å for nitrogen and oxygen and 2.5 Å for carbon. In each case, the *OOH binding energy was higher (−1.21 to −1.33 eV) than that of the bare Co-N₄ (−1.09 eV) and was close to that of bare Fe-N₄ (−1.37 eV). In contrast, under the conditions in which the Co nanoclusters were coordinated, there was a significant reduction in the *OOH binding energy at all distances. These results indicate that the close interaction between the Co-N₄ active site and the organic adducts on the support materials present in the ma-Co-NC catalyst increases the oxophilicity, which in-turn enhances the first PCET step, thereby lowering the probability of 2-electron ORR and renders the 4-electron ORR predominant. Moreover, in the p-Co-NC catalyst, where a large number of Co-NPs exist, the overall oxophilicity is expected to be lower, which adversely affects the ORR activity. For the lowest and highest *OOH binding energies of each model, we derived the free energy profiles of the associative ORR pathway (Fig. 6(c)). As expected, the interaction with organic molecules increased the overall oxophilicity; in particular, *OOH and *OH binding energies were selectively increased over those of *O₂ and *O. Furthermore, it was confirmed that the interaction with Co nanoclusters plays a role in inhibiting ORR activity by significantly lowering the affinity for *OOH and other reaction intermediates. Thus, as summarized in Table S5, organic molecular coordinated systems demonstrated theoretical ORR potential values of

0.67–0.79 V vs. CHE, further enhancing energetics to facilitate 4-electron ORR greater than those for the bare Co-N₄ and even the Fe-N₄ systems. The systematic changes in oxophilicity with respect to the axial coordination environment of the Co-N₄ active site were analyzed based on the electronic structural variations of the Co center. First, the total spin density of the Co center showed a strong linear correlation with the *OOH binding energy, as shown in Fig. 6(d). Bare Co-N₄ had a spin density of approximately 0.90, delocalized on the $d_{xz/yz}$ orbitals, and the coordination with the organic molecules caused electronic structural changes, leading to localization of the spin on d_{z^2} up to a spin density of 1.07. Conversely, coordination with the Co nanocluster reduced the total spin density to 0.05. We rationalized these electronic structure changes by following the concepts of crystal field theory (Fig. 6(e)): 1) When the closed-shell 2p electrons of the organic molecule approached Co-N₄ in the axial direction, the d_{z^2} level of the Co center was strongly destabilized relative to $d_{xz/yz}$, thereby forming a more localized spin structure along the z-direction (Fig. S16). 2) When the $d_{xz/yz}$ and d_{z^2} electrons interacted almost equally between the Co center and Co-NPs, the $d_{xz/yz}$ and d_{z^2} orbitals achieved similar levels of instability and maintained their ordering. In this case, electron transfer from electron-rich (or zero-valent) Co-NPs to the Co center took place, lowering the total spin density (Fig. S17). These electronic structural changes enabled selective increases in *OOH and *OH binding energies, where the sigma-type bonding character dominates between Co d_{z^2} electrons and the single unpaired 2p electrons on the reaction intermediates. Moreover, owing to the nature of the closed-shell electronic structure due to the Co-NP coordination, the overall oxophilicity is inevitably weakened.

4. Conclusions

We employed a melamine-encapsulated Co-doped ZnO composite as

a ZIF-8 precursor to control the metal dispersion and pore structure. Atomic clusters and hierarchical pore ma-Co-NC were successfully synthesized, demonstrating an improved ORR activity under acidic conditions compared to p-Co-NC with Co nanoparticles. The melamine sources played a crucial role in preventing Co aggregation and the formation of mesopores (38 nm). Furthermore, DFT calculations predicted that ma-Co-NC increases oxophilicity with respect to the axial coordination environment of the Co-N₄ active site to enable the 4-electron ORR activity, demonstrating comparable activity to those of the Fe-N₄ sites. The unique structure of the Co-NC catalyst presented in this study will provide excellent insights into the development of non-precious metal-based cathodes of superior performance and durability for application in PEMFCs, as well as for mass production.

CRediT authorship contribution statement

Kyungmin Im: Conceptualization, Methodology, Validation, Formal analysis, Investigation, Writing – original draft, Visualization. **Jue-Hyuk Jang:** Conceptualization, Methodology, Validation, Formal analysis, Investigation, Writing – original draft, Visualization. **Jinseo Heo:** Validation, Formal analysis, Investigation. **Donghui Kim:** Formal analysis, Investigation. **Kug-Seung Lee:** Formal analysis, Investigation. **Hyung-Kyu Lim:** Validation, Formal analysis, Investigation, Writing – review and editing, Supervision. **Jinsoo Kim:** Writing – review and editing, Supervision, Funding acquisition. **Sung Jong Yoo:** Writing – review and editing, Supervision, Funding acquisition.

Declaration of Competing Interest

The authors declare that they have no known competing financial interests or personal relationships that could have appeared to influence the work reported in this paper.

Acknowledgments

K. Im. and Dr. J.-H. Jang. contributed equally to this work.

This work was supported by the National Research Foundation of Korea (NRF) grant funded by the Korea government (2018M1A2A2061975, 2019R1A2C1090693, 2021M3H4A1A02042948, 2021R1A5A6002853) and by the New & Renewable Energy Core Technology Program of KETEP (20203020030010). This work was also supported by the KIST Institutional Program (2Z06370-20-232).

Appendix A. Supporting information

Supplementary data associated with this article can be found in the online version at [doi:10.1016/j.apcatb.2022.121220](https://doi.org/10.1016/j.apcatb.2022.121220).

References

- [1] M.K. Debe, Electrocatalyst approaches and challenges for automotive fuel cells, *Nature* 486 (2012) 43–51.
- [2] S. Ahmadi, S. Bathaee, A.H. Hosseini, Improving fuel economy and performance of a fuel-cell hybrid electric vehicle (fuel-cell, battery, and ultra-capacitor) using optimized energy management strategy, *Energy Convers. Manag.* 160 (2018) 74–84.
- [3] X. Lü, Y. Qu, Y. Wang, C. Qin, G. Liu, A comprehensive review on hybrid power system for PEMFC-HEV: Issues and strategies, *Energy Convers. Manag.* 171 (2018) 1273–1291.
- [4] Z.W. Seh, J. Kibsgaard, C.F. Dickens, I.B. Chorkendorff, J.K. Nørskov, T. F. Jaramillo, Combining theory and experiment in electrocatalysis: Insights into materials design, *Science* 355 (2017).
- [5] G. Wu, K.L. More, C.M. Johnston, P. Zelenay, High-performance electrocatalysts for oxygen reduction derived from polyaniline, iron, and cobalt, *Science* 332 (2011) 443–447.
- [6] S. Yang, J. Kim, Y.J. Tak, A. Soon, H. Lee, Single-atom catalyst of platinum supported on titanium nitride for selective electrochemical reactions, *Angew. Chem. Int. Ed.* 55 (2016) 2058–2062.
- [7] L. Liu, A. Corma, Metal catalysts for heterogeneous catalysis: from single atoms to nanoclusters and nanoparticles, *Chem. Rev.* 118 (2018) 4981–5079.
- [8] X. Yang, A. Wang, B. Qiao, J. Li, J. Liu, T. Zhang, Single-atom catalysts: a new frontier in heterogeneous catalysis, *Acc. Chem. Res.* 46 (2013) 1740–1748.
- [9] E. Luo, H. Zhang, X. Wang, L. Gao, L. Gong, T. Zhao, Z. Jin, J. Ge, Z. Jiang, C. Liu, Single-atom Cr–N₄ sites designed for durable oxygen reduction catalysis in acid media, *Angew. Chem.* 131 (2019) 12599–12605.
- [10] X. Sun, S. Sun, S. Gu, Z. Liang, J. Zhang, Y. Yang, Z. Deng, P. Wei, J. Peng, Y. Xu, High-performance single atom bifunctional oxygen catalysts derived from ZIF-67 superstructures, *Nano Energy* 61 (2019) 245–250.
- [11] X.X. Wang, D.A. Cullen, Y. Pan, S. Hwang, M. Wang, Z. Feng, J. Wang, M. H. Engelhard, H. Zhang, Y. He, Nitrogen-coordinated single cobalt atom catalysts for oxygen reduction in proton exchange membrane fuel cells, *Adv. Mater.* 30 (2018), 1706758.
- [12] H. Zhang, H.T. Chung, D.A. Cullen, S. Wagner, U.I. Kramm, K.L. More, P. Zelenay, G. Wu, High-performance fuel cell cathodes exclusively containing atomically dispersed iron active sites, *Energy Environ. Sci.* 12 (2019) 2548–2558.
- [13] K. Im, D. Kim, J. Jang, J. Kim, S.J. Yoo, Hollow-sphere Co-NC synthesis by incorporation of ultrasonic spray pyrolysis and pseudomorphic replication and its enhanced activity toward oxygen reduction reaction, *Appl. Catal. B Environ.* 260 (2020), 118192.
- [14] K. Im, Q.H. Nguyen, E. Lee, D.W. Lee, J. Kim, S.J. Yoo, High-dispersion Co-Fe-NC electrocatalyst based on leaf-shaped zeolite imidazole framework for oxygen–reduction reaction in acidic medium, *Int. J. Energy Res.* 45 (2021) 15534–15543.
- [15] J. Tang, R.R. Salunkhe, H. Zhang, V. Malgras, T. Ahamad, S.M. Alshehri, N. Kobayashi, S. Tominaka, Y. Ide, J.H. Kim, Ultrastructural characterization of the lower motor system in a mouse model of krabbe disease, *Sci. Rep.* 6 (2016) 1–8.
- [16] N. Cheng, L. Ren, X. Xu, Y. Du, S.X. Dou, Recent development of zeolitic imidazolate frameworks (ZIFs) derived porous carbon based materials as electrocatalysts, *Adv. Energy Mater.* 8 (2018), 1801257.
- [17] C. Wang, J. Kim, J. Tang, M. Kim, H. Lim, V. Malgras, J. You, Q. Xu, J. Li, Y. Yamauchi, New strategies for novel MOF-derived carbon materials based on nanoarchitectures, *Chem* 6 (2020) 19–40.
- [18] M. Zhang, C. Wang, C. Liu, R. Luo, J. Li, X. Sun, J. Shen, W. Han, L. Wang, Metal-organic framework derived Co₃O₄/C@SiO₂ yolk-shell nanoreactors with enhanced catalytic performance, *J. Mater. Chem. A* 6 (2018) 11226–11235.
- [19] C. Hou, L. Zou, L. Sun, K. Zhang, Z. Liu, Y. Li, C. Li, R. Zou, J. Yu, Q. Xu, Single-atom iron catalysts on overhang-eave carbon cages for high-performance oxygen reduction reaction, *Angew. Chem.* 132 (2020) 7454–7459.
- [20] X.F. Lu, Y. Fang, D. Luan, X.W.D. Lou, Metal-organic frameworks derived functional materials for electrochemical energy storage and conversion: a mini review, *Nano Lett.* 21 (2021) 1555–1565.
- [21] L. Shang, H. Yu, X. Huang, T. Bian, R. Shi, Y. Zhao, G.I. Waterhouse, L. Wu, C. Tung, T. Zhang, Well-dispersed ZIF-derived Co,N-Co-doped carbon nanoframes through mesoporous-silica-protected calcination as efficient oxygen reduction electrocatalysts, *Adv. Mater.* 28 (2016) 1668–1674.
- [22] H. Zhou, D. He, A.I. Saana, J. Yang, Z. Wang, J. Zhang, Q. Liang, S. Yuan, J. Zhu, S. Mu, Mesoporous-silica induced doped carbon nanotube growth from metal-organic frameworks, *Nanoscale* 10 (2018) 6147–6154.
- [23] X. Yang, Y. Wang, G. Zhang, L. Du, L. Yang, M. Markiewicz, J. Choi, R. Chenitz, S. Sun, SiO₂-Fe/N/C catalyst with enhanced mass transport in PEM fuel cells, *Appl. Catal. B Environ.* 264 (2020), 118523.
- [24] X. Wan, X. Liu, Y. Li, R. Yu, L. Zheng, W. Yan, H. Wang, M. Xu, J. Shui, Fe–N–C electrocatalyst with dense active sites and efficient mass transport for high-performance proton exchange membrane fuel cells, *Nat. Catal.* 2 (2019) 259–268.
- [25] H.T. Chung, D.A. Cullen, D. Higgins, B.T. Sneed, E.F. Holby, K.L. More, P. Zelenay, Direct atomic-level insight into the active sites of a high-performance PGM-free ORR catalyst, *Science* 357 (2017) 479–484.
- [26] X. Fu, P. Zamani, J. Choi, F.M. Hassan, G. Jiang, D.C. Higgins, Y. Zhang, M. A. Hoque, Z. Chen, In situ polymer graphenization ingrained with nanoporosity in a nitrogenous electrocatalyst boosting the performance of polymer-electrolyte-membrane fuel cells, *Adv. Mater.* 29 (2017), 1604456.
- [27] C.H. Choi, H. Lim, M.W. Chung, G. Chon, N.R. Sahraie, A. Altin, M. Sougrati, L. Stievano, H.S. Oh, E.S. Park, The Achilles' heel of iron-based catalysts during oxygen reduction in an acidic medium, *Energy Environ. Sci.* 11 (2018) 3176–3182.
- [28] Y. Shao, J. Dodelet, G. Wu, P. Zelenay, PGM-free cathode catalysts for PEM fuel cells: a mini-review on stability challenges, *Adv. Mater.* 31 (2019), 1807615.
- [29] E. Jung, H. Shin, B. Lee, V. Efremov, S. Lee, H.S. Lee, J. Kim, W.H. Antink, S. Park, K. Lee, Atomic-level tuning of Co–N–C catalyst for high-performance electrochemical H₂O₂ production, *Nat. Mater.* 19 (2020) 436–442.
- [30] X. Xie, C. He, B. Li, Y. He, D.A. Cullen, E.C. Wegener, A.J. Kropf, U. Martinez, Y. Cheng, M.H. Engelhard, Performance enhancement and degradation mechanism identification of a single-atom Co–N–C catalyst for proton exchange membrane fuel cells, *Nat. Catal.* 3 (2020) 1044–1054.
- [31] L. Chen, X. Liu, L. Zheng, Y. Li, X. Guo, X. Wan, Q. Liu, J. Shang, J. Shui, Insights into the role of active site density in the fuel cell performance of Co–N–C catalysts, *Appl. Catal. B Environ.* 256 (2019), 117849.
- [32] G. Kresse, J. Furthmüller, Efficiency of ab-initio total energy calculations for metals and semiconductors using a plane-wave basis set, *Comput. Mater. Sci.* 6 (1996) 15–50.
- [33] J.P. Perdew, K. Burke, M. Ernzerhof, Generalized gradient approximation made simple, *Phys. Rev. Lett.* 77 (1996) 3865–3868.
- [34] K. Mathew, R. Sundaraman, K. Letchworth-Weaver, T.A. Arias, R.G. Hennig, Implicit solvation model for density-functional study of nanocrystal surfaces and reaction pathways, *J. Chem. Phys.* 140 (2014), 084106.

- [35] Y. Sun, Q. Zhang, X. Xu, L. Zhang, Z. Wu, J. Guo, G. Lu, ZnO@ZIF core-shell single crystals formed by in situ conversion of ZnO particles, *Eur. J. Inorg. Chem.* 2016 (2016) 3553–3558.
- [36] E. Zanchetta, L. Malfatti, R. Ricco, M.J. Styles, F. Lisi, C.J. Coghlan, C.J. Doonan, A. J. Hill, G. Brusatin, P. Falcaro, ZnO as an efficient nucleating agent for rapid, room temperature synthesis and patterning of Zn-based metal-organic frameworks, *Chem. Mater.* 27 (2015) 690–699.
- [37] J. Reboul, S. Furukawa, N. Horike, M. Tsotsalas, K. Hirai, H. Uehara, M. Kondo, N. Louvain, O. Sakata, S. Kitagawa, Mesoscopic architectures of porous coordination polymers fabricated by pseudomorphic replication, *Nat. Mater.* 11 (2012) 717–723.
- [38] L. Jiao, H. Jiang, Metal-organic-framework-based single-atom catalysts for energy applications, *Chem* 5 (2019) 786–804.
- [39] X. Wang, Z. Li, Y. Qu, T. Yuan, W. Wang, Y. Wu, Y. Li, Review of metal catalysts for oxygen reduction reaction: from nanoscale engineering to atomic design, *Chem* 5 (2019) 1486–1511.
- [40] V.P. Glibin, J. Dodelet, Thermodynamic stability in acid media of fen4-based catalytic sites used for the reaction of oxygen reduction in PEM fuel cells, *J. Electrochem. Soc.* 164 (2017) F948–F957.
- [41] V.P. Glibin, M. Cherif, F. Vidal, J. Dodelet, G. Zhang, S. Sun, Non-PGM electrocatalysts for PEM fuel cells: thermodynamic stability and DFT evaluation of fluorinated FeN4-based ORR catalysts, *J. Electrochem. Soc.* 166 (2019) F3277–F3286.
- [42] C.H. Choi, C. Baldizzone, G. Polymeros, E. Pizzutillo, O. Kasian, A.K. Schuppert, N. Ranjbar Sahräie, M. Sougrati, K.J. Mayrhofer, F. Jaouen, Minimizing operando demetallation of Fe-N-C electrocatalysts in acidic medium, *ACS Catal.* 6 (2016) 3136–3146.
- [43] D.K. Lavallee, Kinetics and mechanisms of metalloporphyrin reactions, *Coord. Chem. Rev.* 61 (1985) 55–96.
- [44] D. Banham, T. Kishimoto, Y. Zhou, T. Sato, K. Bai, J. Ozaki, Y. Imashiro, S. Ye, Critical advancements in achieving high power and stable nonprecious metal catalyst-based MEAs for real-world proton exchange membrane fuel cell applications, *Sci. Adv.* 4 (2018) eaar7180.
- [45] J. Li, M. Chen, D.A. Cullen, S. Hwang, M. Wang, B. Li, K. Liu, S. Karakalos, M. Lucero, H. Zhang, Atomically dispersed manganese catalysts for oxygen reduction in proton-exchange membrane fuel cells, *Nat. Catal.* 1 (2018) 935–945.
- [46] J. Zang, F. Wang, Q. Cheng, G. Wang, L. Ma, C. Chen, L. Yang, Z. Zou, D. Xie, H. Yang, Cobalt/zinc dual-sites coordinated with nitrogen in nanofibers enabling efficient and durable oxygen reduction reaction in acidic fuel cells, *J. Mater. Chem. A* 8 (2020) 3686–3691.
- [47] X.X. Wang, D.A. Cullen, Y. Pan, S. Hwang, M. Wang, Z. Feng, J. Wang, M. H. Engelhard, H. Zhang, Y. He, Nitrogen-coordinated single cobalt atom catalysts for oxygen reduction in proton exchange membrane fuel cells, *Adv. Mater.* 30 (2018), 1706758.
- [48] Y. Yin, J. Liu, Y. Chang, Y. Zhu, X. Xie, Y. Qin, J. Zhang, K. Jiao, Q. Du, M. D. Guiver, Design of Pt-C/Fe-N-S-C cathode dual catalyst layers for proton exchange membrane fuel cells under low humidity, *Electrochim. Acta* 296 (2019) 450–457.
- [49] Q. Cheng, S. Han, K. Mao, C. Chen, L. Yang, Z. Zou, M. Gu, Z. Hu, H. Yang, Co nanoparticle embedded in atomically-dispersed Co-N-C nanofibers for oxygen reduction with high activity and remarkable durability, *Nano Energy* 52 (2018) 485–493.
- [50] K. Wang, H. Chen, X. Zhang, Y. Tong, S. Song, P. Tsiakaras, Y. Wang, Rac1 silencing, NSC23766 and EHT1864 reduce growth and actin organization of bladder smooth muscle cells, *Appl. Catal. B Environ.* 264 (2020), 118468.
- [51] X. Zhang, Q. Liu, J. Shui, Non-alcoholic fatty liver disease: a metabolic burden promoting atherosclerosis, *ChemElectroChem* 7 (2020) 1775–1780.
- [52] Y. Deng, X. Tian, B. Chi, Q. Wang, W. Ni, Y. Gao, Z. Liu, J. Luo, C. Lin, L. Ling, Hierarchically open-porous carbon networks enriched with exclusive Fe-Nx active sites as efficient oxygen reduction catalysts towards acidic H₂-O₂ PEM fuel cell and alkaline Zn-air battery, *Chem. Eng. J.* 390 (2020), 124479.
- [53] D. Xia, F. Tang, X. Yao, Y. Wei, Y. Cui, M. Dou, L. Gan, F. Kang, Attenuation calibration method based on sensitivity correction in a Raman distributed temperature system, *Carbon* 162 (2020) 300–307.